

Introducing Highly Redox-Active Atomic Centers into Insertion-Type Electrodes for Lithium-Ion Batteries

Yanjiao Ma, Yuan Ma, Gabriele Giuli,* Holger Euchner, Axel Groß, Giovanni Orazio Lepore, Francesco d'Acapito, Dorin Geiger, Johannes Biskupek, Ute Kaiser, Hanno M. Schütz, Anna Carlsson, Thomas Diemant, Rolf Jürgen Behm, Matthias Kuenzel, Stefano Passerini, and Dominic Bresser*

The development of alternative anode materials with higher volumetric and gravimetric capacity allowing for fast delithiation and, even more important, lithiation is crucial for next-generation lithium-ion batteries. Herein, the development of a completely new active material is reported, which follows an insertion-type lithiation mechanism, metal-doped CeO_2 . Remarkably, the introduction of carefully selected dopants, herein exemplified for iron, results in an increase of the achievable capacity by more than 200%, originating from the reduction of the dopant to the metallic state and additional space for the lithium ion insertion due to a significant off-centering of the dopant atoms in the crystal structure, away from the original Ce site. In addition to the outstanding performance of such materials in high-power lithium-ion full-cells, the selective reduction of the iron dopant under preservation of the crystal structure of the host material is expected to open up a new field of research.

is considered the rate-limiting step.^[3–5] Presently, the strategy of choice consists of a stepwise, preferably complete, replacement of graphite by (understoichiometric) silicon (oxide), theoretically providing enhanced specific energy and power on the full-cell level.^[6] However, this comes at the expense of limited cycle life, as the corresponding alloying reaction is accompanied by pronounced volume variations. These cause cracking of the active material particles, which leads to continuous electrolyte decomposition, increasing cell resistance, and loss of active material.^[7–9] In fact, the most desirable solution would be an electrode material providing little to negligible volume variation upon de/lithiation in combination with a lithium

1. Introduction


The steadily increasing demand for lithium-ion batteries (LIBs) with high energy and power density is triggering the development of new active materials.^[1,2] With respect to a potential rapid charging (<10–15 min), this concerns particularly the replacement of the graphite anode, for which the lithium intercalation

storage capacity and potential similar to (or better than) graphite and, additionally, fast kinetics. Insertion-type materials, thanks to the conserved structural integrity of the crystalline host material when the mobile guest species is entering the available structural sites, are the best candidates.^[10,11] Nonetheless, apart from graphite, only few candidates have been reported so far. $\text{Li}_4\text{Ti}_5\text{O}_{12}$ and TiO_2 have attracted some interest, but suffer

Dr. Y.-J. Ma, Dr. Y. Ma, H. M. Schütz, Prof. R. J. Behm, Dr. M. Kuenzel, Prof. S. Passerini, Dr. D. Bresser
Helmholtz Institute Ulm (HIU)
Ulm D-89081, Germany
E-mail: dominic.bresser@kit.edu

Dr. Y. Ma, Dr. Y. Ma, H. M. Schütz, Dr. M. Kuenzel, Prof. S. Passerini, Dr. D. Bresser
Karlsruhe Institute of Technology (KIT)
Karlsruhe D-76021, Germany

Prof. G. Giuli
School of Science and Technology – Geology Division
University of Camerino
Camerino 62032, Italy
E-mail: gabriele.giuli@unicam.it

 The ORCID identification number(s) for the author(s) of this article can be found under <https://doi.org/10.1002/aenm.202000783>.

© 2020 The Authors. Published by WILEY-VCH Verlag GmbH & Co. KGaA, Weinheim. This is an open access article under the terms of the Creative Commons Attribution License, which permits use, distribution and reproduction in any medium, provided the original work is properly cited.

Dr. H. Euchner, Prof. A. Groß
Institute of Theoretical Chemistry
Ulm University
Ulm D-89081, Germany

Dr. G. O. Lepore, Dr. F. d'Acapito
CNR-IOM-OGG
Grenoble 38043, France

Dr. D. Geiger, Dr. J. Biskupek, Prof. U. Kaiser
Central Facility for Electron Microscopy
Ulm University
Ulm D-89081, Germany

Dr. A. Carlsson
Thermo Fisher Scientific
Eindhoven NL-5651, Netherlands

Dr. T. Diemant, Prof. R. J. Behm
Institute of Surface Chemistry and Catalysis
Ulm University
Ulm D-89081, Germany

DOI: 10.1002/aenm.202000783

from substantially lower capacities (about half that of graphite) and higher operative voltages (1.5–1.7 V).^[12–15] This results in a decrease in energy density by a factor of 3–4 on the full-cell level. Another insertion-type material that, however, has attracted only little attention so far is CeO₂ due to the following reasons: First, CeO₂ is more expensive than titanates (even though cerium is as abundant as copper^[16]) and, second, the insertion-type capacity is rather limited, i.e., ≈155 mAh g⁻¹ when considering a maximum lithium uptake of one Li⁺ per CeO₂. Furthermore, the precise reaction mechanism is still under debate.^[17–19] For our proof-of-concept study, however, it provides a distinct advantage, as it does not undergo any phase transition upon de/lithiation. This allows us to rule out any potential impact of such structural rearrangement, therefore facilitating the overall investigation and interpretation of the results.

In this study, we show that the introduction of selected metal dopants, exemplarily illustrated for iron, occupying an off-centered

position in the CeO₂ crystal structure, allows for a dramatic increase in capacity by more than 200%. The key to such an improvement lies in the reduction of the dopant atoms to the metallic state without affecting the crystalline host structure. Such a mechanism—to the best of our knowledge—is reported herein for the first time. Fe-doped CeO₂ negative electrodes coupled with high-voltage LiNi_{0.5}Mn_{1.5}O₄ positive electrodes provide high-power LIBs with excellent cycling stability and gravimetric energy and power densities up to 200 Wh kg⁻¹ and 8500 W kg⁻¹, respectively.

2. Results and Discussion

2.1. Synthesis and Physicochemical Characterization

Figure 1a presents the X-ray diffraction (XRD) patterns of CeO₂ and Ce_{0.9}Fe_{0.1}O₂. All reflections are typical for the cubic CeO₂

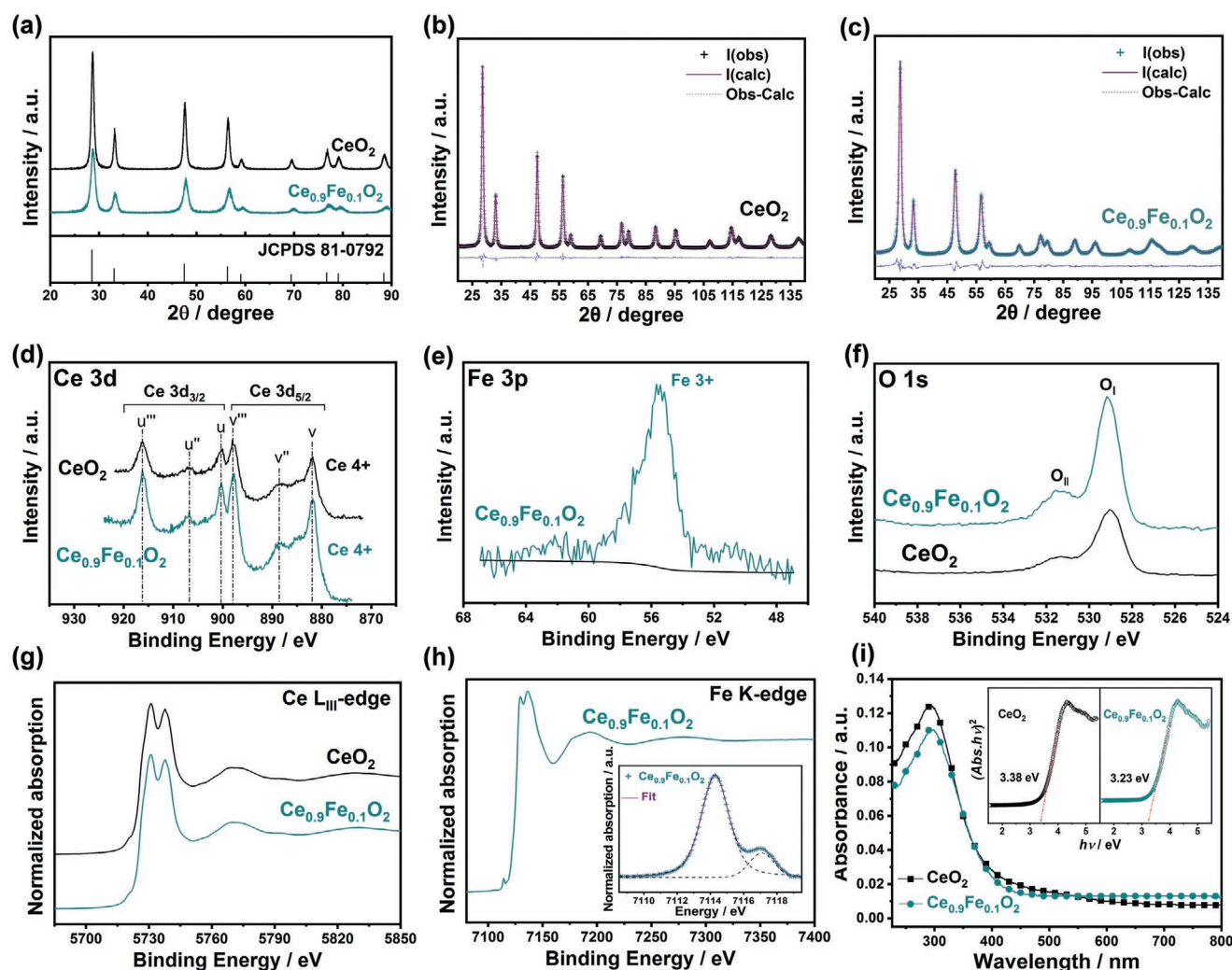


Figure 1. a) X-ray diffraction (XRD) patterns of CeO₂ (in black) and Fe-doped CeO₂ (Ce_{0.9}Fe_{0.1}O₂, in cyan); the JCPDS card No. 81–0792 of the fluorite cubic structure is given as reference in the bottom; b–c) Rietveld refined diffractograms of (b) CeO₂ and (c) Ce_{0.9}Fe_{0.1}O₂; d–f) X-ray photoelectron spectroscopy (XPS) analysis of pure CeO₂ and Ce_{0.9}Fe_{0.1}O₂. d) Comparison of the Ce 3d spectra for both samples, and comparison of the O 1s spectra for both samples (f). g–h) Normalized X-ray absorption spectroscopy (XAS) spectra collected at the (g) Ce L_{III} edge for both samples and (h) Fe K edge for Ce_{0.9}Fe_{0.1}O₂ (inset: background-subtracted Fe pre-edge peak). i) Ultraviolet-visible (UV–vis) absorption spectra for pure CeO₂ and Ce_{0.9}Fe_{0.1}O₂; as inset the corresponding plots for the determination of the band gap.

structure ($Fm\bar{3}m$ space group, JCPDS reference 81–0792), indicating the formation of crystalline CeO_2 . The absence of any Ce and/or Fe-bearing impurities suggests that Fe was successfully incorporated into the CeO_2 lattice. The Rietveld refinement (Figure 1b,c and Table S1, Supporting Information) provides an accurate determination of the unit cell parameters and atomic positions. The introduction of the iron dopant results in an increasing full width at half maximum (FWHM) of the recorded reflections, indicating a slight decrease in crystallite size (20 versus 18 nm), accompanied by a significant decrease of the unit cell volume. X-ray photoelectron spectroscopy (XPS; see Figure S1a,b, Supporting Information, for the survey spectra) confirmed the presence of cerium and oxygen in both samples and iron in $\text{Ce}_{0.9}\text{Fe}_{0.1}\text{O}_2$. A detailed comparison of these two samples is provided in Figure 1d–f, revealing that Ce is purely tetravalent^[20,21] in both cases, while Fe is trivalent^[21,22] in $\text{Ce}_{0.9}\text{Fe}_{0.1}\text{O}_2$ (see Supporting Information for a detailed discussion of the spectra). For a further analysis of the oxidation states and local structure, we performed X-ray absorption spectroscopy (XAS) measurements, collecting data at both the Ce L_{III} -edge and Fe K-edge. The XANES spectra at the Ce L_{III} -edge of CeO_2 and $\text{Ce}_{0.9}\text{Fe}_{0.1}\text{O}_2$ (Figure 1g) confirm that Ce has the same local environment in both phases.^[23] The position and the shape of the main absorption edge indicate that Ce is in its tetravalent state (Figure S2a, Supporting Information).

Furthermore, results from the EXAFS region, which can be fitted according to the model obtained from the XRD data, and the unit cell parameters as estimated on the basis of the Ce–O distance, are in good agreement with the results obtained by XRD (Figure S2b,c, Table S2, and Table S3, Supporting Information). The pre-edge feature of the Fe-doped compound in the Fe K-edge XANES spectrum (Figure 1h) infers the presence of Fe^{3+} , compatible with a noncentrosymmetric bonding environment. This aliovalent Fe doping results in a slightly reduced band gap of 3.23 eV compared to 3.38 eV for pure CeO_2 , in good agreement with previous findings,^[24,25] and thus an increased electronic conductivity (Figure 1i)—presumably also due to the presence of oxygen vacancies to balance the incorporation of the aliovalent dopant. In fact, a comparison of the Raman spectra recorded for Fe-doped CeO_2 , self-synthesized CeO_2 , and commercial CeO_2 (serving as additional reference) reveals a clear indication for an increased presence of oxygen vacancies as a consequence of the Fe doping (Figure S3, Supporting Information). Nonetheless, as we cannot quantify the amount of oxygen vacancies, we will continue referring to $\text{Ce}_{0.9}\text{Fe}_{0.1}\text{O}_2$ rather than the theoretically expected composition of $\text{Ce}_{0.9}\text{Fe}_{0.1}\text{O}_{1.95}$ in the following text.

The two materials were characterized also by (high-resolution) transmission electron microscopy ((HR)TEM; Figure 2). The TEM micrographs for pure CeO_2 reveal a cubic

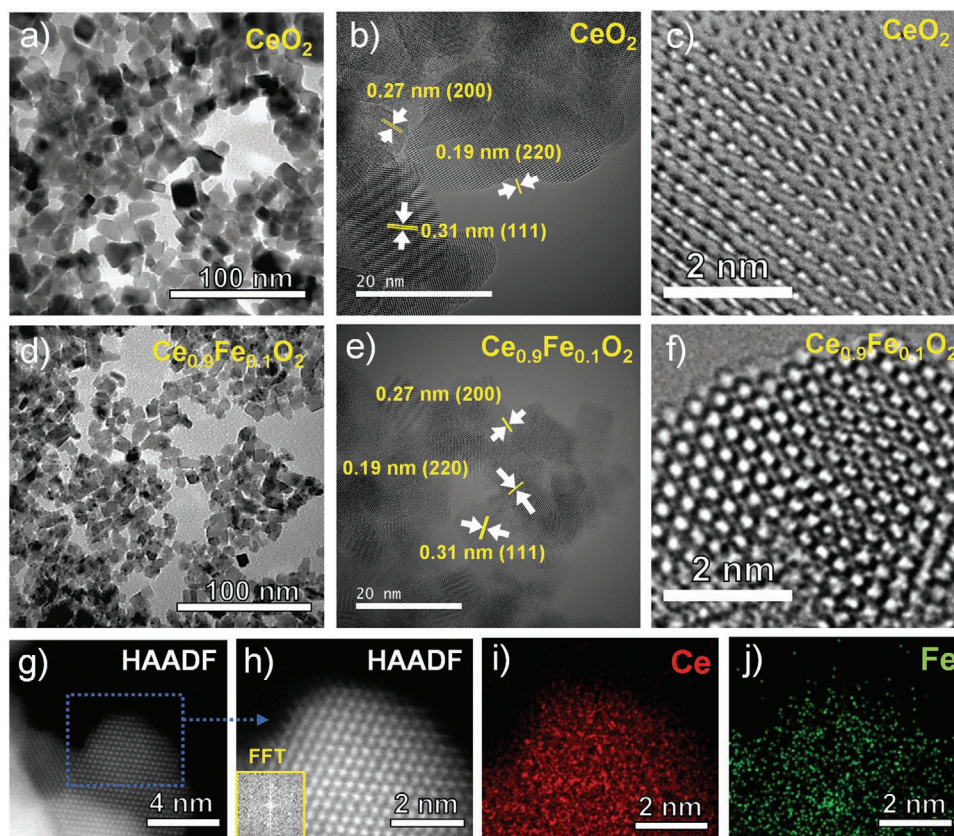


Figure 2. TEM–HRTEM (where TEM is transmission electron microscopy and HRTEM is high-resolution transmission electron microscopy) micrographs of (a–c) CeO_2 and (d–f) $\text{Ce}_{0.9}\text{Fe}_{0.1}\text{O}_2$. g,h) High-angle annular dark-field scanning transmission electron microscopy (HAADF–STEM) micrographs of an exemplary $\text{Ce}_{0.9}\text{Fe}_{0.1}\text{O}_2$ particle in [110] orientation. The rectangle in (g) shows the area for the subsequent local energy-dispersive X-ray spectroscopy (EDX) mapping for Ce and Fe presented in (i) and (j), respectively. The reflections in the FFT pattern, shown as inset in the HAADF-reference map in panel (h), verifies near-atomic EDX mapping. The extracted elemental maps in (i) and (j) show the distribution of Ce and Fe, respectively, within the exemplary $\text{Ce}_{0.9}\text{Fe}_{0.1}\text{O}_2$ particle.

particle shape with an average diameter of around 16 nm, whereas the introduction of Fe into the CeO_2 lattice results in a decreased particle size of around 12 nm (Figure 2a,d), which is in good agreement with the XRD results. The corresponding (HR)TEM micrographs (Figure 2b,e) nicely confirm the synthesis of well-crystallized nanoparticles with the characteristic lattice fringes of 0.31, 0.27, and 0.19 nm for the fluorite-related (111), (200), and (220) planes, respectively. Moreover, the fluorite-structured $\text{Ce}_{0.9}\text{Fe}_{0.1}\text{O}_2$ material does not show any apparent secondary phases, further confirming the successful incorporation of the iron dopant into the CeO_2 structure (Figure 2c,f). The well-crystallized structure of the $\text{Ce}_{0.9}\text{Fe}_{0.1}\text{O}_2$ nanoparticles was also confirmed by conducting high-angle annular dark-field scanning transmission electron microscopy (HAADF-STEM) together with parallel energy-dispersive X-ray spectroscopy (EDX) for spatially resolved element analysis. Figure 2g shows an atomically resolved HAADF image of an exemplary $\text{Ce}_{0.9}\text{Fe}_{0.1}\text{O}_2$ particle in [110] orientation. The rectangle in Figure 2g marks the area of a local EDX mapping to determine the elemental composition of this particle. The near-atomically resolved element mapping (verified by the crystal reflection of the FFT taken from the HAADF reference (inset in Figure 2h)) shows a uniform and atomic-level distribution of Ce and, more importantly, Fe within the nanocrystal (Figure 2i,j, respectively). The quantification of the elemental ratio between Ce and Fe resulted in a value of 9.5:1 which is in very good agreement with the intended ratio of 9:1 and the ratio obtained by inductively coupled plasma optical emission spectroscopy (ICP-OES), revealing a ratio of (9.3:1 for Ce:Fe).

2.2. Electrochemical Characterization with Li Counter Electrodes

For the electrochemical characterization, CeO_2 and $\text{Ce}_{0.9}\text{Fe}_{0.1}\text{O}_2$ based electrodes were subjected to galvanostatic cycling (Figure 3). The first cycle potential profiles are provided in Figure S4a, Supporting Information. The CeO_2 electrodes show a reversible capacity of about 168 mAh g^{-1} when applying a specific current of 0.02 A g^{-1} . In the subsequent cycles, however, the specific capacity is gradually fading and finally stabilizes at 82 mAh g^{-1} for a specific current of 0.05 A g^{-1} (Figure 3a). This decrease is mainly due to the loss of reversible capacity at higher voltages (i.e., above 1.0 V), as apparent from the dis-/charge profiles (Figure 3b) and, additionally, the cyclic voltammetry (CV) measurements (Figure S4b, Supporting Information).

Doping CeO_2 with Fe results in a substantially enhanced specific capacity of 305 mAh g^{-1} in the first cycle (Figure S4a, Supporting Information), which subsequently stabilizes at around 260 mAh g^{-1} (Figure 3a), reflecting an increase of more than 200% compared to pure CeO_2 . Remarkably, in contrast to pure CeO_2 , there is no significant capacity fading in the initial cycles, as illustrated by the almost perfect overlap of the dis-/charge profiles (Figure 3b) and the CV sweeps (Figure S4c, Supporting Information). Such a superior capacity performance also translates into much better rate capability as shown in Figure 3c, with the corresponding dis-/charge profiles depicted in Figure 3d. Electrodes based on $\text{Ce}_{0.9}\text{Fe}_{0.1}\text{O}_2$ reveal higher specific capacities for all applied specific currents, ranging from 0.05 A g^{-1} to 5.0 A g^{-1} . For example, at a very high current of 5 A g^{-1} , $\text{Ce}_{0.9}\text{Fe}_{0.1}\text{O}_2$ still provides a capacity of about 70 mAh g^{-1} compared to only 30 mAh g^{-1} for CeO_2 . Moreover, when

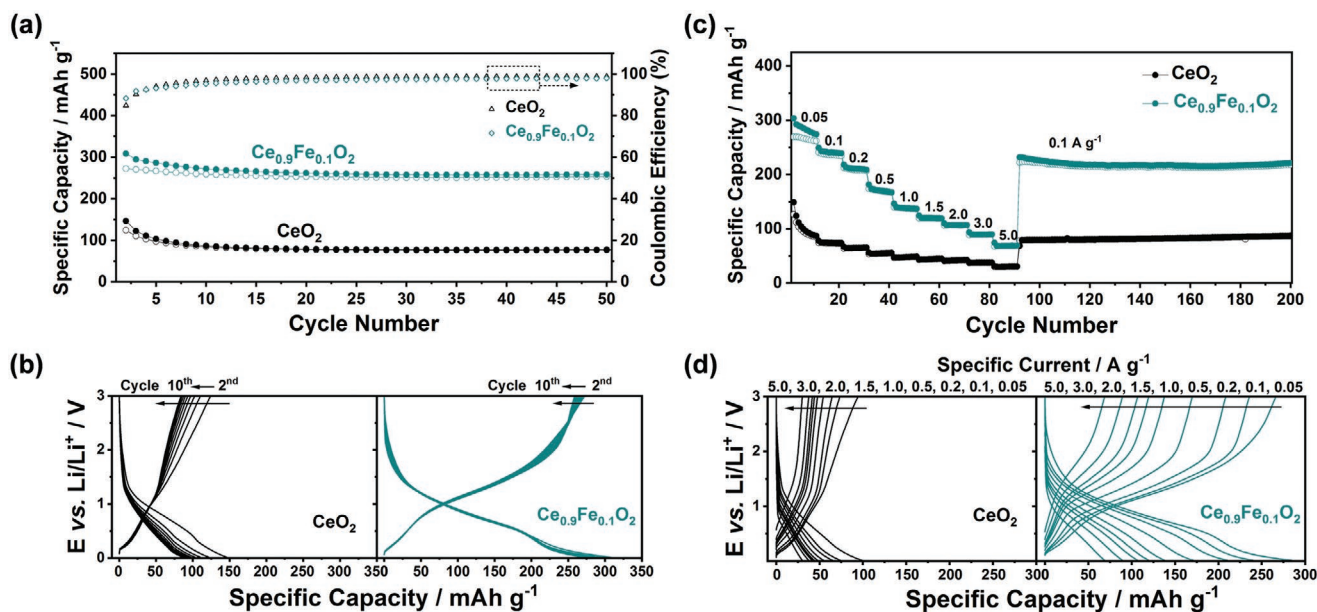


Figure 3. a,b) Galvanostatic cycling of electrodes based on CeO_2 (in black) and $\text{Ce}_{0.9}\text{Fe}_{0.1}\text{O}_2$ (in cyan). a) Constant current cycling at 50 mA g^{-1} , plotting the specific dis-/charge capacity and coulombic efficiency versus the cycle number (1st cycle not shown). b) The corresponding dis-/charge profiles for the 2nd–10th cycle of CeO_2 (left) and $\text{Ce}_{0.9}\text{Fe}_{0.1}\text{O}_2$ (right). c,d) Multirate galvanostatic cycling of electrodes based on CeO_2 and $\text{Ce}_{0.9}\text{Fe}_{0.1}\text{O}_2$. c) Dis-/charge capacity versus cycle number at 0.05, 0.1, 0.2, 0.5, 1.0, 1.5, 2.0, 3.0, and 5.0 A g^{-1} , subsequently getting back to 0.1 A g^{-1} . d) The corresponding dis-/charge profiles for the fifth cycle at each specific current for CeO_2 (left) and $\text{Ce}_{0.9}\text{Fe}_{0.1}\text{O}_2$ (right).

lowering the current to 0.1 A g⁻¹, the doped material provides a capacity of 224 mAh g⁻¹, which is still about thrice as high as for CeO₂ (78 mAh g⁻¹), underlining again the excellent reversibility of the de-/lithiation reaction in Ce_{0.9}Fe_{0.1}O₂. Noteworthy, this increase in capacity is directly correlated to the concentration of the Fe dopant. Lowering the Fe ratio from 0.1 to 0.05 (i.e., Ce_{0.95}Fe_{0.05}O₂) leads to a significant decrease in capacity, i.e., a reversible capacity of 209 mAh g⁻¹ in the first cycle, which subsequently stabilizes at around 180 mAh g⁻¹ (Figure S5, Supporting Information). This increase in reversible capacity is about half the increase when introducing 0.1 Fe, further corroborating the important contribution of the Fe dopant to the superior capacity.

2.3. Elucidating the Reaction Mechanism and Impact of the Fe Dopant

To investigate the impact of the Fe dopant on the de-/lithiation mechanism and, thus, to understand the reason for the enhanced performance, we used a highly complementary set of different techniques, starting with the in situ XRD analysis of CeO₂ and Ce_{0.9}Fe_{0.1}O₂ based electrodes (Figure 4a,b). For both measurements, we present the corresponding waterfall diagrams and the contour plots of the recorded XRD patterns in combination with the simultaneously recorded two dis-/charge cycles. For CeO₂ (Figure 4a), the evolution of the XRD patterns reveals a continuous shift of the fluorite-related (111), (200), (220), and (311) reflections to lower 2θ values due to the increasing unit cell volume upon lithiation, accompanied by a slight broadening of the reflections and decrease in intensity. During the subsequent charge the reflections shift back to the initial 2θ values and increase in intensity, though remaining slightly lower as compared to the initial pattern. For the second dis-/charge cycle, we observe exactly the same behavior, indicating a highly reversible de-/lithiation. In fact, no new phase is observed, demonstrating that the lithiation occurs solely by solid-solution de-/insertion (in agreement with previous in situ XRD results^[17]), while the slight decrease in crystallinity is assigned to extended lattice expansion during the first lithiation. For Fe-doped CeO₂ (Figure 4b), the evolution of the XRD patterns shows essentially the same trend. However, the shift to lower angles is dramatically increased, indicating a substantial increase in unit cell volume resulting from more lithium cations being reversibly inserted, which is in excellent agreement with the extensive capacity increase. For a detailed analysis, we also conducted an ex situ analysis of pristine, discharged (0.01 V), and charged (3.0 V) CeO₂ and Ce_{0.9}Fe_{0.1}O₂ electrodes (Figure S6 and Table S2, Supporting Information). Comparing the cubic lattice parameter a_0 for pure and Fe-doped CeO₂ in the pristine and lithiated state reveals an increase from 5.418(1) to 5.545(1) Å and from 5.396(1) to 5.683(1) Å, respectively, which is in line with the remarkable shift of the (111) and the (200) diffraction peaks shown in Figure S6b (Supporting Information; CeO₂) and Figure S6d (Supporting Information; Ce_{0.9}Fe_{0.1}O₂). Remarkably, delithiated CeO₂ reveals a minor fraction of Ce₂O₃ (similar to a previous study^[18]), which is not observed for Ce_{0.9}Fe_{0.1}O₂. These findings further support our conclusion that the Fe doping leads to a substantially larger

amount of Li⁺ being reversibly inserted into the crystalline lattice. As a matter of fact, the crystal structure is very well preserved after a complete dis-/charge cycle as confirmed by the ex situ HRTEM micrographs depicted in Figure 4c,d. Cycled Ce_{0.9}Fe_{0.1}O₂ reveals the same lattice fringes as the pristine sample, i.e., 0.31, 0.27, and 0.19 for the (111), (200), and (220) planes, respectively (Figure 4c), as well as an essentially perfect atomic ordering even at the very edge of the particle (Figure 4d). To complement this study, ex situ XAS analysis was performed. XANES spectra were recorded at the Ce L_{III}-edge of CeO₂ and Ce_{0.9}Fe_{0.1}O₂ before and after lithiation and are presented in Figure 4e,f and Figure S2a (Supporting Information). For both cases, the XANES data clearly show a complete reduction of Ce⁴⁺ to Ce³⁺ (Figure S2a, Supporting Information). Moreover, the EXAFS fits (Table S3 and Figure S2b,c, Supporting Information) performed on the first coordination shell of the lithiated samples confirm the reduction of Ce, showing a marked increase of the Ce–O distance (Table S3, Supporting Information) in good agreement with XRD data (Table S2, Supporting Information). The reduction occurs also for the Fe dopant, as highlighted by the comparison of the XANES regions measured on pristine and lithiated Ce_{0.9}Fe_{0.1}O₂ at the Fe K-edge, indicating the reduction of Fe to the metallic state (Figure 4g). The quantitative EXAFS analysis has also been performed at the Fe K-edge (Figure 4h,i and Table S3, Supporting Information). The results for the pristine sample are in agreement with the analyses of the pre-edge and XANES regions. Specifically, Fe shows a first coordination shell containing ≈5 oxygen atoms with an average Fe–O bond distance of 1.97(1) Å. A weak second shell signal, corresponding to a small bump at ≈3.3 Å is resolved in Figure 4i. This feature is satisfactorily modeled by a mixed Ce/Fe shell with Fe and Ce atoms at 2.96(1) and 3.45(1) Å, respectively. The rather short Fe–O distance and the low coordination number suggest that Fe does not substitute Ce at the center of the CeO₈ cube, but occupies a significantly off-centered position, close to one face of the CeO₈ cube. To the best of our knowledge such a coordination geometry has never been reported for Fe³⁺ in inorganic compounds. The metallic character of Fe in the lithiated sample is evident when comparing the length of the EXAFS oscillation in Figure 4h and the relative Fourier Transform (FT) profile (Figure 4i) with that of the pristine sample. Fit results indicate a first shell mainly composed of Fe atoms with a Fe–Fe bond distance of 2.42(1) Å. The shoulder at the low-R side of the main FT peak, though, can be modeled in the EXAFS multiparameter fit as a Fe–O bond, suggesting that the first shell comprises Fe and O, which prevents us from an accurate estimation of the coordination number. Interestingly, the Fe–Fe interatomic distance is significantly shorter than the one observed in BCC Fe (2.48 Å), indicating that Fe in the lithiated sample forms extremely small subnanometric clusters.^[26,27] Such shortening can be explained in terms of surface stress due to the higher surface to volume ratio in the clusters.^[28] Montano et al.^[26,29] studied Fe clusters isolated in solid argon via EXAFS, observing a gradual reduction of the Fe–Fe distance as the cluster size decreased. The Fe–Fe distance was close to 2.40 Å in oligo-clusters with a mean diameter of 9 Å. They also noticed that the 9 Å particle size marks a threshold between clusters showing a BCC structure and a less ordered structure compatible with an FCC or HCP lattice. In

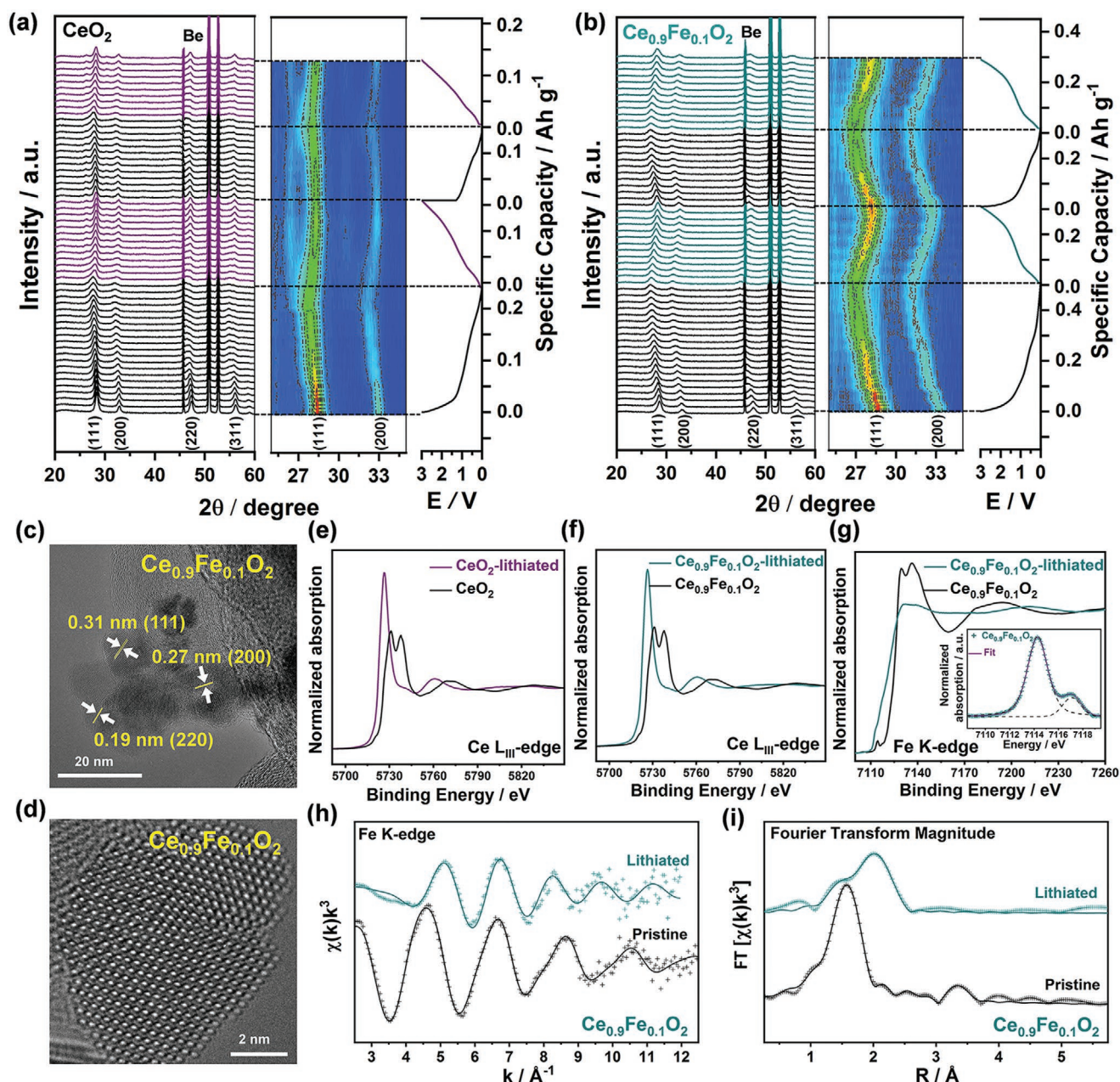


Figure 4. a) In situ X-ray diffraction (XRD) analysis of pure CeO_2 : Waterfall diagrams (left) and contour plots (middle; the different coloring in red and blue represents the lowest and highest relative intensity of the XRD peaks, respectively) of consecutively recorded XRD patterns as well as the corresponding galvanostatic dis-/charge profiles for the first two de-/lithiation cycles (right; specific current: 10 mA g^{-1} ; cut-off voltages: 0.01 and 3.0 V versus Li/Li^+). b) In situ XRD analysis of $\text{Ce}_{0.9}\text{Fe}_{0.1}\text{O}_2$: Waterfall diagrams (left) and contour plots (middle; see panel (a) for the color coding) of consecutively recorded XRD patterns as well as the corresponding galvanostatic dis-/charge profiles for the first two de-/lithiation cycles (right; specific current: 20 mA g^{-1} ; cut-off voltages: 0.01 and 3.0 V versus Li/Li^+). c, d) Ex situ transmission electron microscopy (TEM) and high-resolution transmission electron microscopy (HRTEM) micrograph, respectively, of $\text{Ce}_{0.9}\text{Fe}_{0.1}\text{O}_2$ subjected to one complete dis-/charge cycle. e–g) Ex situ XANES data obtained for CeO_2 and $\text{Ce}_{0.9}\text{Fe}_{0.1}\text{O}_2$: Comparison of the normalized XANES spectra collected at the Ce L_{III} -edge for the pristine material and after discharge to 0.01 V for (e) CeO_2 and (f) $\text{Ce}_{0.9}\text{Fe}_{0.1}\text{O}_2$. g) Comparison of the normalized XANES spectra collected for $\text{Ce}_{0.9}\text{Fe}_{0.1}\text{O}_2$ at the Fe K-edge for the pristine material and after discharge to 0.01 V (inset: background subtracted Fe pre-edge peak). h–i) Ex situ EXAFS spectra and corresponding multiparameter fit for pristine and discharged $\text{Ce}_{0.9}\text{Fe}_{0.1}\text{O}_2$ (cyan and black lines, respectively). h) The Fe K-edge k^3 -weighted EXAFS region of $\text{Ce}_{0.9}\text{Fe}_{0.1}\text{O}_2$. i) The Fourier transforms (uncorrected for phase shifts) of the EXAFS for $\text{Ce}_{0.9}\text{Fe}_{0.1}\text{O}_2$.

our case, no Fe second shell signal can be observed, indicating the lack of an ordered structure, which fits well with the earlier mentioned presence of a mixed O/Fe first shell and the

small value for the Fe–Fe distance; all being in agreement with the hypothesis of very small subnanometric Fe clusters.^[30,31] According to Fritsche and Benfield,^[30] a coordination number

close to 3 would indeed be compatible with a Fe tetramer with tetrahedral geometry. Our EXAFS results therefore suggest that Fe in the lithiated sample is mainly present as an extremely small cluster, presumably a dimer or tetramer (including a minor interaction with the surrounding oxygen). Considering that the crystalline structure of cerium oxide is well preserved upon reduction of Fe to the metallic state (Figure 4c,d), the mixed Fe/O first shell in the lithiated state, and the mixed Ce/Fe shell in the pristine state, we propose the following model: Beside the very homogeneous Fe distribution observed at the scale of Figure 2j, there are presumably always two Fe^{3+} cations in direct vicinity, which is, in fact, reasonable regarding the need to balance the aliovalent doping induced point defects (similar to Fe-doped $\text{ZnO}^{[32,33]}$). In the reduced state, these iron atoms experience an increased attractive interaction, thus getting closer, without, however, destroying the crystalline host structure. In such a way, the available sites for lithium cations are increased.

To further deepen our understanding of the reaction mechanism, density functional theory (DFT) based calculations on pure and Fe-doped CeO_2 were conducted. In agreement with the experimental data, Ce in CeO_2 is eightfold coordinated by oxygen, resulting in a cubic environment (Figure 5a). However,

as the atomic radius of Fe is about 25% smaller than the one of Ce, the Fe–O distances in the eightfold-coordinated position are too large to allow for strong Fe–O interaction. Rather, a shift of Fe toward the face center of the surrounding oxygen cube is observed, resulting in fourfold coordinated Fe with shorter Fe–O distances. This scenario is depicted in Figure 5a for supercells of pure and Fe-doped CeO_2 , where in case of the Fe-doping one Ce atom per supercell is replaced by Fe (corresponding to ≈ 3 at% Fe doping). The configuration with fourfold-coordinated Fe is energetically more stable by >2 eV. It should be noted that the Fe–O bond distance of 1.83 \AA is somewhat smaller than the experimental value, which may be a consequence of the different doping levels (i.e., 3 at% versus 10 at%). Apart from being energetically more favorable, the shift of the dopant away from the cube center provides additional space in the structure that may enable the insertion of further Li. For more insight, we investigated pure and Fe-doped CeO_2 structures with different degrees of lithiation. First, we compared half-lithiated ordered-like structures with 0.5 Li per formula unit (Figure 5b). The non-doped compound is unstable with respect to a decomposition into Li-metal and CeO_2 (in agreement with the structural instability non-doped CeO_2 upon lithiation, resulting in the formation of Ce_2O_3 as discussed

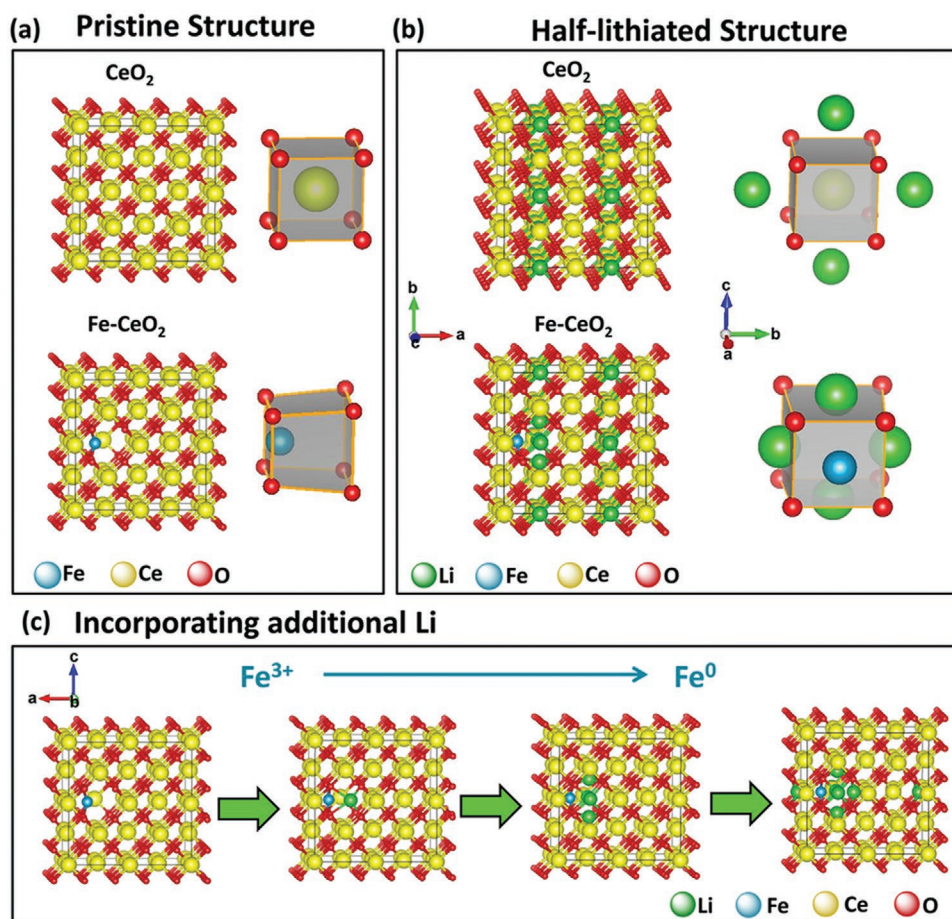


Figure 5. a) Crystal structure of pure CeO_2 and Fe-doped CeO_2 and the local environments corresponding to both cases. b) Prototype structure for a half-lithiated (i.e., 0.5 Li per unit formula), ordered, Fe-free CeO_2 , and Fe-doped structure. c) Prototype structures for incorporating additional Li within the structure of Fe-doped CeO_2 .

earlier), whereas the doped compound is stable with respect to the elemental constituents. When introducing 1 Li into the Fe-doped CeO_2 lattice (Figure 5c), the inserted Li is preferably located in the vicinity of the Fe dopant.

Moreover, Bader charge analysis as well as the magnetic moment of iron clearly indicate the reduction of iron (see Table S4, Supporting Information). The addition of further Li per supercell results in the accumulation of additional charge on the Fe atom. Only once Fe approaches the Fe^0 oxidation state, significant changes of the Bader charges on the Ce sites are observed. Together with the evolution of the magnetic moment of Fe, this strongly indicates a reduction of Fe^{3+} to Fe^0 (see Supporting Information for the detailed discussion). Our findings clearly support the experimentally observed improved Li uptake of the Fe-doped compound as compared to pure CeO_2 and corroborate the surprising reduction of Fe to its metallic state.

Considering that the complete reduction of Fe and the reduction of Ce^{4+} to Ce^{3+} correspond to a theoretical total lithium uptake of 1.2 Li per formula unit $\text{Ce}_{0.9}\text{Fe}_{0.1}\text{O}_2$, a theoretical capacity of 196 mAh g^{-1} would be expected. This value, however, is lower than the experimentally determined specific capacity. To understand this aspect, we conducted a comparative kinetic analysis of the lithium storage process for CeO_2 and $\text{Ce}_{0.9}\text{Fe}_{0.1}\text{O}_2$ using CV to determine the ratio of the diffusion- and pseudocapacitive contribution to the overall capacity. Figure 6a,b displays the CV data for CeO_2 and $\text{Ce}_{0.9}\text{Fe}_{0.1}\text{O}_2$. The general shape is well preserved upon increasing the sweep rate from 0.05 to 2.0 mV s^{-1} . Utilizing the equation $i(V) = k_1 v + k_2 v^{1/2}$ (see Supporting Information for a detailed discussion), we find that at a scan rate of $1.0 \text{ mV s}^{-1} \approx 79\%$ of the charge storage for CeO_2 arises from pseudocapacitive processes (Figure 6c), while it is “only” 57% in case of $\text{Ce}_{0.9}\text{Fe}_{0.1}\text{O}_2$ (Figure 6d). In fact, the pseudocapacitive contribution is sub-

stantially higher for pure CeO_2 across all applied sweep rates (Figure 6e), reaching 85% for CeO_2 and 73% for $\text{Ce}_{0.9}\text{Fe}_{0.1}\text{O}_2$ at 2.0 mV s^{-1} , indicating that the slightly smaller particle size and, thus, larger surface area of the Fe-doped material does not lead to a greatly extended pseudocapacitive charge storage (especially relatively speaking, while it may slightly increase, indeed, when considering absolute values—see also the following comparison at the end of this paragraph). Generally, though, the small particle size presumably contributes to the excellent rate performance.^[34,35] Even more important for the understanding of the lithiation mechanism, the rather high pseudocapacitive contribution even at low sweep rates (e.g., 44% and 30% for CeO_2 and $\text{Ce}_{0.9}\text{Fe}_{0.1}\text{O}_2$ at 0.05 mV s^{-1} , respectively) provides an explanation for the significantly higher specific capacity values compared to the theoretical maxima, i.e., about 160 and 305 mAh g^{-1} compared to <78 ($\text{Li}_{<0.5}\text{CeO}_2$) and 196 mAh g^{-1} for CeO_2 and Fe-doped CeO_2 , respectively. As a matter of fact, in case of $\text{Ce}_{0.9}\text{Fe}_{0.1}\text{O}_2$, the complete reduction of Ce^{4+} to Ce^{3+} and Fe^{3+} to Fe^0 corresponds to a capacity contribution of 196 mAh g^{-1} , while the pseudocapacitive contribution at such low rates is about 30%, i.e., the remaining $\approx 100 \text{ mAh g}^{-1}$.

2.4. Enhancing the Performance by Applying a Carbon Coating

Focusing on the electrochemical performance, we added a carbon coating to $\text{Ce}_{0.9}\text{Fe}_{0.1}\text{O}_2$ (denoted as $\text{Ce}_{0.9}\text{Fe}_{0.1}\text{O}_2\text{-C}$) using a rather simple, but effective method based on glucose as carbon precursor.^[36,37] The final carbon content was determined via TGA to be $\approx 16 \text{ wt\%}$ (Figure S7, Supporting Information). Comparison of the XRD pattern with those of pure CeO_2 and noncoated $\text{Ce}_{0.9}\text{Fe}_{0.1}\text{O}_2$ (Figure 7a) shows that the additional processing did not affect the crystal structure.

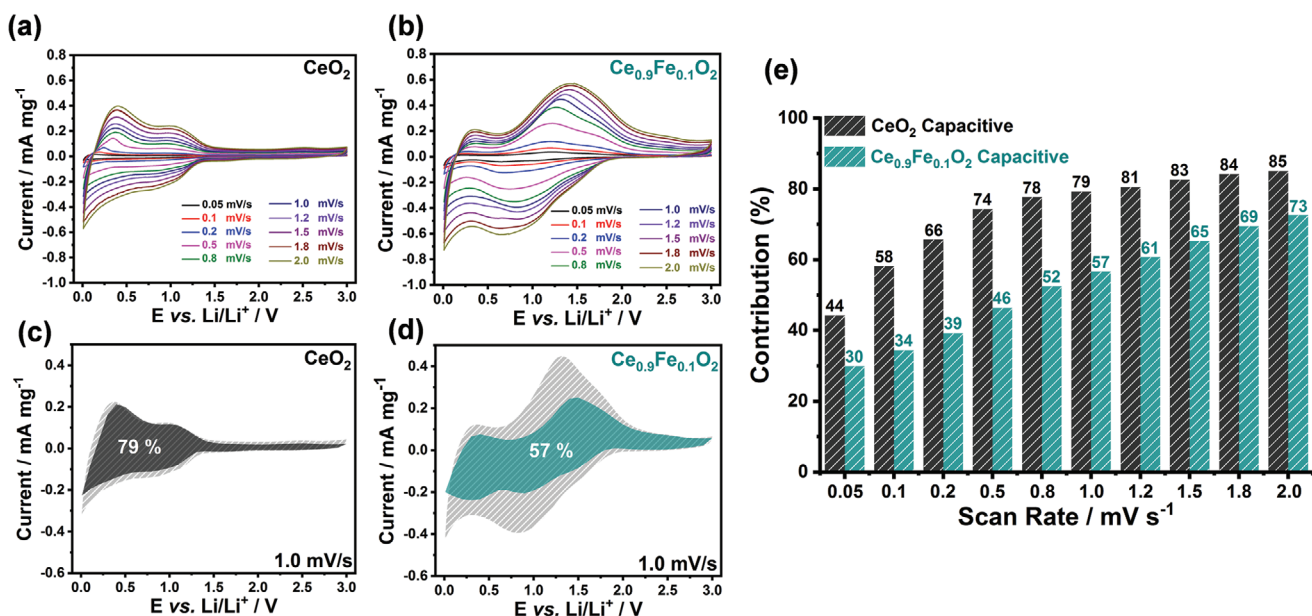


Figure 6. Kinetic analysis of the lithium storage contributions for CeO_2 and $\text{Ce}_{0.9}\text{Fe}_{0.1}\text{O}_2$. a,b) Cyclic voltammograms for electrodes based on (a) CeO_2 and (b) $\text{Ce}_{0.9}\text{Fe}_{0.1}\text{O}_2$ at different sweep rates. c,d) Illustration of the capacitive contribution for (c) CeO_2 (black area) and (d) $\text{Ce}_{0.9}\text{Fe}_{0.1}\text{O}_2$ (cyan area) in comparison to the diffusion-controlled contribution (light gray area in both cases) to the overall charge storage at 1.0 mV s^{-1} . e) Comparison of the percentage of the capacitive contribution to the overall recorded capacity at different scan rates for CeO_2 (in black) and $\text{Ce}_{0.9}\text{Fe}_{0.1}\text{O}_2$ (in cyan).

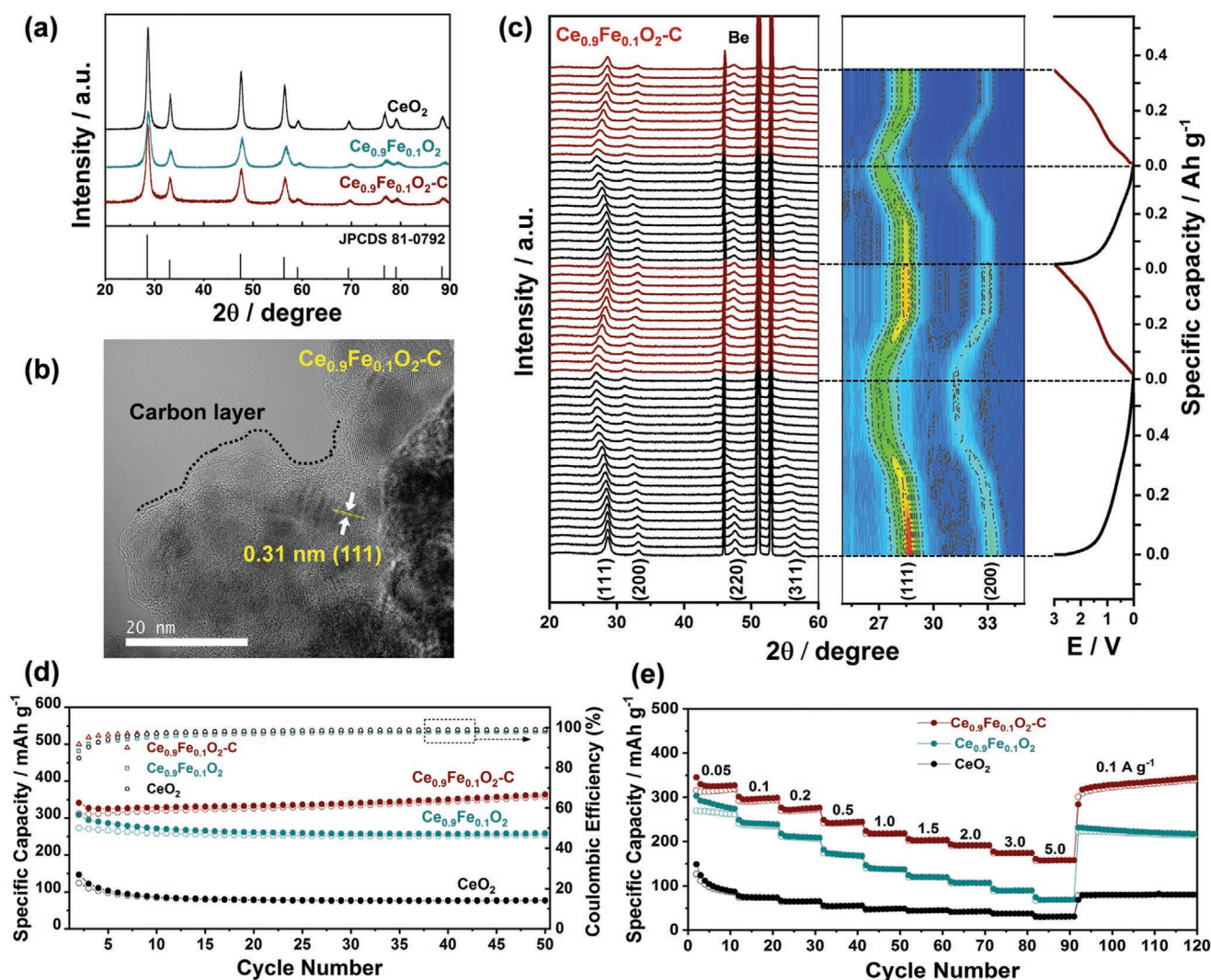


Figure 7. Characterization of carbon-coated $\text{Ce}_{0.9}\text{Fe}_{0.1}\text{O}_2$ ($\text{Ce}_{0.9}\text{Fe}_{0.1}\text{O}_2\text{-C}$). a) X-ray diffraction (XRD) patterns of $\text{Ce}_{0.9}\text{Fe}_{0.1}\text{O}_2\text{-C}$, $\text{Ce}_{0.9}\text{Fe}_{0.1}\text{O}_2$, and CeO_2 . b) High-resolution transmission electron microscopy (HRTEM) micrograph of $\text{Ce}_{0.9}\text{Fe}_{0.1}\text{O}_2\text{-C}$. c) In situ XRD analysis: Waterfall diagram (left) and contour plot (middle); the different coloring in red and blue represents the lowest and highest relative intensity of the XRD peaks, respectively) of consecutively recorded XRD patterns as well as the corresponding galvanostatic dis-/charge profiles for the first two de-/lithiation cycles (right; specific current: 25 mA g^{-1} ; cut-off voltages: 0.01 and 3.0 V versus Li/Li^+). d) Galvanostatic cycling of electrodes based on $\text{Ce}_{0.9}\text{Fe}_{0.1}\text{O}_2\text{-C}$ in comparison with $\text{Ce}_{0.9}\text{Fe}_{0.1}\text{O}_2$ and CeO_2 (plot of the specific dis-/charge capacity and coulombic efficiency versus the cycle number (1st cycle: 20 mA g^{-1} , following cycles 50 mA g^{-1})). e) Rate capability tests by applying elevated specific currents to electrodes based on $\text{Ce}_{0.9}\text{Fe}_{0.1}\text{O}_2\text{-C}$ (once again, the results for $\text{Ce}_{0.9}\text{Fe}_{0.1}\text{O}_2$ and CeO_2 are shown for a direct comparison as well), plotted as the specific dis-/charge capacity versus the cycle number at 0.05, 0.1, 0.2, 0.5, 1.0, 1.5, 2.0, 3.0, and 5.0 A g^{-1} before decreasing the current back to 0.1 A g^{-1} . All specific current and capacity values reported herein are based on the mass of the total composite, i.e., including the carbon coating.

In line with this, the HRTEM micrograph presented in Figure 7b reveals the same lattice fringes as the as-synthesized $\text{Ce}_{0.9}\text{Fe}_{0.1}\text{O}_2$. In addition, the HRTEM analysis reveals the presence of a thin ($\approx 5 \text{ nm}$) carbon layer on the outer surface of the secondary particles, as highlighted by the dashed black line, which simultaneously interconnects the primary nanocrystals. In situ XRD analysis of the electrodes based on $\text{Ce}_{0.9}\text{Fe}_{0.1}\text{O}_2\text{-C}$ to (Figure 7c) reveals generally the same trend as for the non-coated material, with one slight difference: The shift to lower 2θ values upon lithiation is more pronounced in this case, suggesting an even greater lithium storage capacity—presumably due to the increased electronic conductivity induced by the

carbon coating. In fact, subjecting $\text{Ce}_{0.9}\text{Fe}_{0.1}\text{O}_2\text{-C}$ based electrodes to constant (Figure 7d) and elevated current (Figure 7e) cycling reveals a clear improvement in terms of reversibly achievable capacity across all specific currents applied. $\text{Ce}_{0.9}\text{Fe}_{0.1}\text{O}_2\text{-C}$ shows a stable specific capacity of 350 mAh g^{-1} over 50 cycles at 50 mA g^{-1} , which is 1.3 and 4.5 times higher than that of $\text{Ce}_{0.9}\text{Fe}_{0.1}\text{O}_2$ and CeO_2 , respectively. Even at 5 A g^{-1} $\text{Ce}_{0.9}\text{Fe}_{0.1}\text{O}_2\text{-C}$ provides the remarkable capacity of about 160 mAh g^{-1} compared to 70 and 30 mAh g^{-1} for $\text{Ce}_{0.9}\text{Fe}_{0.1}\text{O}_2$ and CeO_2 , respectively. The comparison of the corresponding dis-/charge profiles (Figure S8, Supporting Information) shows that this is partially related to the reduced polarization

and IR drop. But also the de-/insertion dynamics appear to be improved, especially when comparing the profiles recorded for $\text{Ce}_{0.9}\text{Fe}_{0.1}\text{O}_2$ (Figure S8b, Supporting Information) and $\text{Ce}_{0.9}\text{Fe}_{0.1}\text{O}_2\text{-C}$ (Figure S8c, Supporting Information).

2.5. High-Performance $\text{Ce}_{0.9}\text{Fe}_{0.1}\text{O}_2\text{-C}/\text{LiNi}_{0.5}\text{Mn}_{1.5}\text{O}_4$ Full-Cells

Finally, we coupled (pre-cycled) $\text{Ce}_{0.9}\text{Fe}_{0.1}\text{O}_2\text{-C}$ anodes with high-voltage $\text{LiNi}_{0.5}\text{Mn}_{1.5}\text{O}_4$ (LNMO) cathodes to realize LIBs with a suitable full-cell voltage and high power density to benefit from the excellent rate capability of $\text{Ce}_{0.9}\text{Fe}_{0.1}\text{O}_2\text{-C}$ (Figure 8a). Such $\text{Ce}_{0.9}\text{Fe}_{0.1}\text{O}_2\text{-C}/\text{LNMO}$ full-cells show an initial specific discharge capacity of $\approx 85 \text{ mAh g}^{-1}$ (based on the mass of LNMO; 10th cycle) at 1C in a voltage range of 1.0–4.4 V (Figure 8b). Even at 10C—meaning that the cell is dis-/charged in less than 6 min—with a slightly extended voltage range of 0.5–4.5 V, the cell still provides an excellent performance with a high specific capacity of 71 mAh g^{-1} after 200 cycles and a coulombic efficiency of about 99.8%. The corresponding dis-/charge profiles recorded for the 11th, 100th, and 200th cycle (Figure 8c; all at 10C) further illustrate the very good capacity retention and the average discharge voltage of 3.2 V. Motivated by these promising results, we investigated the rate capability in more detail by applying a whole range of C rates (Figure 8d; 1.0–4.0 V). In fact, $\text{Ce}_{0.9}\text{Fe}_{0.1}\text{O}_2\text{-C}/\text{LNMO}$ full-cells provide specific capacities of 97, 95, 92, 89, 86, and 82 mAh g^{-1} at C/3, C/2, 1C, 2C, 3C, and 5C, respectively. Even at very high rates of 10C, 20C, and 30C, the full-cell still exhibits specific capacities of 74, 65, and 58 mAh g^{-1} , respectively. And at least as important, the full-cell showed also an excellent cycling stability when decreasing the

C rate back to C/3, providing a capacity of 105 mAh g^{-1} after 340 cycles.

To compare these results with literature, focusing especially on high-power devices such as fast-charge LIBs^[38–41] and lithium-ion capacitors (LICs),^[42–45] we plotted the given specific energy and power at different C rates in a Ragone-type plot (Figure 8e). Obviously, the $\text{Ce}_{0.9}\text{Fe}_{0.1}\text{O}_2\text{-C}/\text{LNMO}$ full-cell outperforms the LIB and LIC references. Even at an extremely high specific power of 8.5 kW kg^{-1} , such a LIB cell still delivers a specific energy of 111 Wh kg^{-1} . Notably, the maximum power values provided by $\text{Ce}_{0.9}\text{Fe}_{0.1}\text{O}_2\text{-C}/\text{LNMO}$ full-cells are similar or even exceeding those of very recently reported LICs,^[42–45] while providing significantly higher specific energies (see also the detailed comparison provided in Table S6, Supporting Information), rendering it very suitable for high-power applications.

3. Conclusions

The introduction of redox-active dopants into insertion-type active materials is a very promising strategy to maintain the advantages of the insertion mechanism, while simultaneously increasing the lithium storage capability—in our case by more than 200%. We have shown that this beneficial effect results from both the reduction of the off-centered Fe dopant to the metallic state, which occurs without affecting the crystalline host structure, and the additional available space for Li^+ . Coupling this new active material with high-voltage $\text{LiNi}_{0.5}\text{Mn}_{1.5}\text{O}_4$ as cathode provides high-power LIBs with excellent cycling stability and gravimetric energy and power densities of $>200\text{--}110 \text{ Wh kg}^{-1}$ and $105\text{--}8500 \text{ W kg}^{-1}$, respectively. While

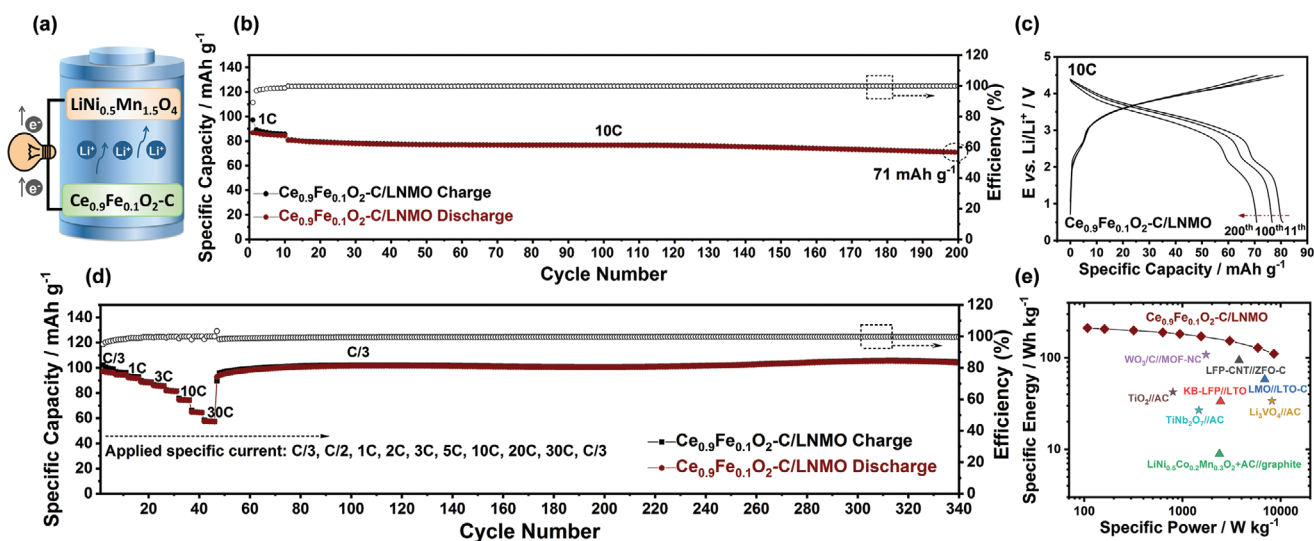


Figure 8. Electrochemical performance of $\text{Ce}_{0.9}\text{Fe}_{0.1}\text{O}_2\text{-C}/\text{LNMO}$ Li-ion full-cells with an anode/cathode capacity ratio of around 1.2–1.3 (at 1C), subjected to galvanostatic cycling (all capacity values given herein refer to the cathode active material). a) Schematic presentation of the full-cell configuration. b,c) Constant current cycling for 200 cycles at 10C after 10 formation cycles at 1C (voltage range: 1.0–4.4 V for the first 10 cycles and 0.5–4.5 V for the following cycles) with (b) the plot of the specific dis-/charge capacity and coulombic efficiency versus the cycle number and (c) the corresponding full-cell dis-/charge profiles for the 11th, 100th, and 200th cycle at 10C. d) Multirate galvanostatic cycling, plotting the dis-/charge capacity versus the cycle number at C/3, C/2, 1C, 2C, 3C, 5C, 10C, 20C, and 30C before getting back to C/3 (voltage range: 1.0–4.4 V). e) Ragone-type plot, providing a comparison of the specific energy and power of the $\text{Ce}_{0.9}\text{Fe}_{0.1}\text{O}_2\text{-C}/\text{LNMO}$ lithium-ion full-cell presented herein (based on the mass of the anode and cathode active material) and earlier reported lithium-ion batteries (LIBs; marked with colored triangles) as well as lithium-ion capacitors (LIC; marked with colored asterisks). The corresponding data are also listed in Table S6, Supporting Information.

this result by itself is already remarkable, we may anticipate that particularly the highly reversible, selective reduction of the dopant on the atomic scale within the maintained crystalline CeO₂ lattice will allow for reconsidering the introduction of (transition) metal dopants in insertion-type battery materials and, ideally, also for the investigation of metallic atoms and their general properties as such when being confined in physically stable host structures.

4. Experimental Section

Materials Synthesis: Fe-doped CeO₂ (Ce_{0.9}Fe_{0.1}O₂) was synthesized by dissolving 1 mmol Fe(NO₃)₃·9H₂O (Alfa Aesar) and 9 mmol of Ce(NO₃)₃·6H₂O (Sigma-Aldrich) in 80 mL deionized water. After stirring the solution for 1 h at room temperature, an aqueous solution of 5 mol L⁻¹ NaOH (Sigma-Aldrich) was used to adjust the pH to ≈14 under constant magnetic stirring. The resulting product was stirred for one more hour and then transferred into a stainless steel autoclave (BERGHOF BR-100) and heated to 200 °C for 24 h under stirring (1000 rpm). The precipitate was collected by centrifugation, washed several times with deionized water and ethanol, and eventually dried at 60 °C overnight. The pure CeO₂ was prepared analogously without adding the Fe precursor.

For carbon coating, 1.2 g glucose (Sigma-Aldrich) was dissolved in 80 mL deionized water before adding 600 mg of the corresponding active material (Ce_{0.9}Fe_{0.1}O₂) under continuous stirring. The resulting suspension was transferred into a stainless steel autoclave (BERGHOF BR-100) and heated to 180 °C for 13 h under stirring (1000 rpm). The precipitate was collected by centrifugation, washed several times with deionized water and ethanol, and finally dried at 60 °C overnight. Subsequently, the dry composite was heated to 400 °C for 2 h under argon atmosphere (heating rate: 3 °C min⁻¹).

Physicochemical Characterization: The crystal structure of the samples was investigated via powder XRD, using either a Bruker D8 Advance (Cu-K_{α1} radiation, λ = 0.154 nm) or an automated Philips Bragg-Brentano diffractometer equipped with a graphite monochromator. For the latter, the long-fine focus Cu tube was operated at 40 kV and 25 mA. Diffractograms were recorded in the 2θ range 18–140° with a 0.02° step and 9 s counting time. The structures were refined with the program GSAS.^[46] The reflections' shape was modeled with a Pseudo-Voigt function; the FWHM was refined as a function of 2θ, taking into account both Gaussian and Lorentzian broadening. The refinement was carried out in the space group and the starting atomic coordinates were those of Artini et al.^[47] with the initial value for the isotropic temperature factors (U_{iso}) arbitrarily chosen as 0.025 Å and then refined. The oxygen sites were assumed as fully occupied, while constraints for fractional occupancies for Ce and Fe were used, according to the stoichiometry of the synthesized samples. The background was modeled with a polynomial function with nine terms. The cell parameters, scale factor, and the background polynomial function were free variables during the refinement. The parameters were added to the refinement in the following order: 2θ zero-shift, peak shape, peak asymmetry, atomic coordinates, and isotropic thermal factor. The intensity cut-off for the calculation of the profile step intensity was initially set at 1.0% of the peak maximum. In the final stages of the refinement, it was lowered to 0.1% of the peak maximum. Final convergence was assumed to be reached when the parameter shifts were <1% of their respective estimated standard deviation. XPS measurements were carried out on a PHI 5800 Multi Technique ESCA system (Physical Electronic, USA). The spectra were acquired using monochromatic Al K_α (1486.6 eV) radiation, a take-off angle of 45°, and pass energies at the electron analyzer of 29.35 and 93.9 eV for the detail and survey scans, respectively. The main C1s peak was used for the binding energy calibration and set to 284.8 eV, corresponding to adventitious carbon on the surface of the powder samples. XAS measurements were performed at the LISA beamline

(BM-08)^[48] at the European Synchrotron Radiation Facility (ESRF, Grenoble, France) at the K-edge and L₃-edge of Fe and Ce, respectively. Samples were measured using a pair of Si (311) flat monochromator crystals, providing an energy resolution of ≈4 × 10⁻⁵ (ΔE/E). This corresponds to an incoming beam energy width of ≈0.3 eV at 7 keV. Si-coated focusing mirrors (E_{cut-off} ≈ 16 keV) were used for harmonic rejection, providing a beam of a roughly circular spot with a diameter of ≈200 μm. Measurements were performed in transmission mode at the Ce L_{III}-edge and in fluorescence mode by means of a 12-element solid state (high purity germanium) detector^[49] at the Fe K-edge. The step size for the pre-edge (for measurements at the Fe K-edge) and in the XANES region was 0.1 and 0.3 eV, respectively. The post-edge EXAFS region of the spectrum was acquired with a fixed k step width of 0.03 Å⁻¹. Measurements were carried out at room temperature. Standard procedures^[50] were followed to extract the structural EXAFS signal (k·χ(k)): pre-edge background removal, spline modeling of bare atomic background, edge step normalization using a far above the edge region, and energy calibration using the software ATHENA.^[51] Model atomic clusters centered on the absorber atom were obtained by ATOMS;^[52] theoretical amplitude and phase functions were generated using the FEFF8 code.^[53] EXAFS spectra were fitted through the ARTEMIS software^[51] in the Fourier Transform (FT) space. UV–vis DRS spectra were recorded with a UV–vis spectrophotometer (Shimadzu UV-2600). The band gap was calculated using the following equation:^[54]

$$\alpha h\nu = A(h\nu - E_g)^{n/2} \quad (1)$$

where E_g is the optical energy band gap, hν is the photon energy, α is the absorption coefficient, and A is a proportionality constant; n is equal to 1 for a direct gap and equal to 4 for an indirect gap. The values of E_g for direct and indirect transitions can be obtained by linear relation and extrapolation. The particle morphology was studied by TEM (JEOL JEM-3000) and HRTEM (image C_s-corrected FEI Titan 80–300 kV at 300 kV). HAADF–STEM was conducted using a Thermo Fisher Titan Themis Z equipped with a probe-corrector (S-COR) and operated at 60 kV. To lower the effect of chromatic aberrations, the energy width of the Schottky electron source was lowered from 0.8 to 0.3 eV by slight excitation of the monochromator. Drift-corrected elemental mappings were acquired using an EDX detector (Thermo Fisher SuperX). Typical mapping times for the EDS analysis were about 10 min using multiple drift-corrected single scans (512 × 512 pixels). ICP–OES was performed on a Spectro Acros-SOP system. For the ICP–OES analysis, 10 mg of each sample was dissolved in hot hydrochloric acid and subsequently diluted with deionized water before performing the measurement. Thermogravimetric analysis (TGA; TA Instruments Q5000) was performed at a heating rate of 5 °C min⁻¹ under O₂ atmosphere. Raman spectroscopy was carried out with a confocal Raman microscope (InVia Renishaw) in the spectral range of 100–1000 cm⁻¹ using a 633 nm laser excitation source and a power of 25 mW. Each spectrum was taken as the average of 30 accumulations with 60 s of acquisition.

Electrode Preparation: The Ce_{0.9}Fe_{0.1}O₂(-C) and CeO₂ based electrodes were composed of the active material (75 wt%), conductive carbon (Super C65, TIMCAL, 20 wt%), and sodium carboxymethyl cellulose (CMC, Dow Wolff Cellulosics, 5 wt%). For the slurry preparation, CMC was dissolved in ultrapure water (1.25 wt% solution) and subsequently Super C65 and the active material were added. The resulting mixture was dispersed by planetary ball milling for 2 h. The resulting electrode paste was cast on dendritic copper foil (Schlenk, 99.9%) using a laboratory doctor blade (wet film thickness: 120 μm). After drying overnight at room temperature, disk-shaped electrodes (12 mm in diameter) were cut and dried under vacuum at 120 °C for 24 h. The active material mass loading of each disk electrode ranged between 1.3 and 1.6 mg cm⁻². The LiNi_{0.5}Mn_{1.5}O₄ (LNMO) cathode material used for the full-cell assembly has been described in our previous work.^[55] The LNMO-based electrodes were prepared by mixing the corresponding active material (80 wt%), conductive carbon (Super C65, TIMCAL, 15 wt%), and polyvinylidene fluoride (PVDF 6020, Solvay, 5 wt%) in N-methyl-2-pyrrolidone (NMP, Aldrich). The resulting slurry was cast on aluminum foil using a laboratory doctor blade (wet film

thickness: 60 μm). The wet electrodes were immediately dried at 60 $^{\circ}\text{C}$ to remove the NMP, then punched to obtain disk electrodes ($\varnothing = 12 \text{ mm}$), which were further vacuum-dried at 150 $^{\circ}\text{C}$ for 12 h. The active material mass loading (LNMO) was about 2.2 mg cm^{-2} .

Electrochemical Measurements: The electrochemical performance was evaluated either in CR2032 coin cells or in Swagelok-type three-electrode cells using lithium foil (Honjo, battery grade) as counter and reference electrodes. All cells were assembled in an argon-filled glove box (MBraun UNIlab, H_2O and O_2 content < 0.1 ppm). The electrolyte consisted of a 1 M solution of LiPF_6 in ethylene carbonate/diethyl carbonate (EC/DEC, 3:7 by volume). Prior to the electrochemical characterization, the cells were allowed to rest for 6 h. CV was carried out using a VMP3 potentiostat (BioLogic), applying 0.01 and 3.0 V as reversing potentials. Galvanostatic cycling tests were performed by means of a battery tester (Maccor 4300), setting the cut-off voltages to 0.01 and 3.0 V versus Li/Li^+ for the half-cell experiments. It is important to note that the mass of the carbon coating for $\text{Ce}_{0.9}\text{Fe}_{0.1}\text{O}_2\text{-C}$ was included for the calculation of the specific capacity. For the full-cells, the $\text{Ce}_{0.9}\text{Fe}_{0.1}\text{O}_2\text{-C}$ anodes were first preactivated in half-cells (Swagelok-type), which were galvanostatically (dis-)charged for 20 cycles and finally charged to 1.75 V in the 20th cycle. Subsequently, the cells including the preactivated $\text{Ce}_{0.9}\text{Fe}_{0.1}\text{O}_2\text{-C}$ were disassembled in a glove box (MBraun UNIlab) and the electrodes were washed with fresh electrolyte before assembling the $\text{Ce}_{0.9}\text{Fe}_{0.1}\text{O}_2\text{-C/LNMO}$ full-cells. The cut-off voltages for the full-cell tests were set to 1.0–4.4 or 0.5–4.5 V, as indicated in the text. All electrochemical measurements were performed in thermostatic climatic chambers at a temperature of 20 ± 1 $^{\circ}\text{C}$.

In Situ XRD Analysis: The in situ XRD experiments were carried out employing a self-designed in situ cell.^[56] The composition of the electrodes was the same as for those used for the electrochemical characterization described above. In this case, however, the electrode paste was cast directly on the beryllium (Be) disk (wet film thickness: 250 μm), acting simultaneously as current collector and “window” for the X-ray beam. The coated Be electrode was dried at 50 $^{\circ}\text{C}$ under vacuum for 12 h. Lithium foil served as counter and reference electrode, while glass fiber sheets (GF/D, Whatman) soaked with 300 μL of the electrolyte were used as separator. The in situ cell was allowed to rest for 12 h before starting the measurement. Galvanostatic cycling was performed using a potentiostat/galvanostat (SP-150, BioLogic) and applying a specific current of 10, 20, and 25 mA g^{-1} for CeO_2 , $\text{Ce}_{0.9}\text{Fe}_{0.1}\text{O}_2$, and $\text{Ce}_{0.9}\text{Fe}_{0.1}\text{O}_2\text{-C}$, respectively (cut-off potentials: 0.01 and 3.0 V). XRD analysis was carried out in a 2θ range of 20–80 $^{\circ}$ with a time per scan of around 30 min.

Ex Situ TEM Analysis: For the ex situ TEM characterization of $\text{Ce}_{0.9}\text{Fe}_{0.1}\text{O}_2$, half-cells were subjected to one full dis-/charge cycle at 20 mA g^{-1} and subsequently opened in an argon-filled glove box. The electrodes were rinsed with DMC to remove any residual electrolyte and dried in the glove box. Small amounts of the electrode coating were scratched off and dispersed in DMC. The solution was drop-casted onto holey carbon films mechanically supported by a copper-mesh (standard 3 mm TEM grid). The DMC solvent was removed under argon atmosphere prior to the transfer of the specimen to the vacuum of the TEM.

Ex Situ XANES and EXAFS Analysis: For the ex situ XANES and EXAFS analysis of $\text{Ce}_{0.9}\text{Fe}_{0.1}\text{O}_2$ and CeO_2 , half-cells were discharged at 20 mA g^{-1} to 0.01 V and then opened in an argon-filled glove box. The electrodes were rinsed with DMC to remove any residual electrolyte, then dried and sealed within polyethylene (PE) foil to avoid any potential air contamination during the transport to the synchrotron and during the measurement.

DFT Calculations: DFT calculations have been conducted with the Vienna ab initio simulation package (VASP).^[57] VASP is a periodic plane wave code, in which the electron–ion interaction is described by pseudopotentials for effective computation. Spin-polarized calculations were conducted using the projector augmented wave method,^[58] while the exchange and correlation were accounted for by the generalized gradient approximation in the formulation of Perdew, Burke, and Ernzerhof.^[59] All structures investigated are based on a $2 \times 2 \times 2$

supercell of the CeO_2 archetype structure and were optimized with respect to atomic positions and lattice parameters using a plane wave energy cut-off of 600 eV and a $4 \times 4 \times 4$ k-point mesh. For the determination of the oxidation states, Bader charges and magnetic moments were analyzed.^[60–63]

Supporting Information

Supporting Information is available from the Wiley Online Library or from the author.

Acknowledgements

Financial support from the Chinese Scholarship Council (CSC; Y.-J.M. and Y.M.), the Vector Foundation within the framework of the NEW E² project, and the Helmholtz Association is kindly acknowledged. Part of this work was performed on the supercomputer ForHLR, funded by the Ministry of Science, Research and the Arts Baden-Württemberg and by the Federal Ministry of Education and Research. Furthermore, the authors would like to thank Oliver Mendoza Reyes and Ruihao Gong for conducting the UV–vis experiments including the very valuable discussion. LISA CRG staff is kindly acknowledged for the provision of in-house beamtime on BM08. The authors also acknowledge DESY (Hamburg, Germany), a member of the Helmholtz Association HGF, for the provision of experimental facilities. Part of this research was carried out at PETRA III, and the authors would like to thank P65 staff for the assistance during measurements.

Conflict of Interest

The authors declare no conflict of interest.

Keywords

batteries, doping, insertion mechanisms, lithium-ion anodes, lithium-ion batteries

Received: February 29, 2020

Revised: April 12, 2020

Published online:

- [1] E. C. Evarts, *Nature* **2015**, 526, S93.
- [2] J. B. Goodenough, *Nat. Electron.* **2018**, 1, 204.
- [3] Y. Yamada, Y. Iriyama, T. Abe, Z. Ogumi, *Langmuir* **2009**, 25, 12766.
- [4] N. Loeffler, D. Bresser, S. Passerini, M. Copley, *Johnson Matthey Technol. Rev.* **2015**, 59, 34.
- [5] D. Bresser, K. Hosoi, D. Howell, H. Li, H. Zeisel, K. Amine, S. Passerini, *J. Power Sources* **2018**, 382, 176.
- [6] J. W. Choi, D. Aurbach, *Nat. Rev. Mater.* **2016**, 1, 16013.
- [7] C.-M. Park, J.-H. Kim, H. Kim, H.-J. Sohn, *Chem. Soc. Rev.* **2010**, 39, 3115.
- [8] M. N. Obrovac, V. L. Chevrier, *Chem. Rev.* **2014**, 114, 11444.
- [9] D. Bresser, S. Passerini, B. Scrosati, *Energy Environ. Sci.* **2016**, 9, 3348.
- [10] V. Aravindan, Y.-S. Lee, S. Madhavi, *Adv. Energy Mater.* **2015**, 5, 1402225.
- [11] H. Li, X. Liu, T. Zhai, D. Li, H. Zhou, *Adv. Energy Mater.* **2013**, 3, 428.
- [12] Z. Chen, I. Belharouak, Y.-K. Sun, K. Amine, *Adv. Funct. Mater.* **2013**, 23, 959.

- [13] T.-F. Yi, L.-J. Jiang, J. Shu, C.-B. Yue, R.-S. Zhu, H.-B. Qiao, *J. Phys. Chem. Solids* **2010**, *71*, 1236.
- [14] D. Bresser, E. Paillard, E. Binetti, S. Krueger, M. Striccoli, M. Winter, S. Passerini, *J. Power Sources* **2012**, *206*, 301.
- [15] D. Bresser, E. Paillard, M. Copley, P. Bishop, M. Winter, S. Passerini, *J. Power Sources* **2012**, *219*, 217.
- [16] A. A. Yaroshevsky, *Geochem. Int.* **2006**, *44*, 48.
- [17] C. Hua, X. Fang, Z. Yang, Y. Gao, Z. Wang, L. Chen, *Electrochem. Commun.* **2012**, *25*, 66.
- [18] Q. Su, L. Chang, J. Zhang, G. Du, B. Xu, *J. Phys. Chem. C* **2013**, *117*, 4292.
- [19] K. Li, X. Zhou, A. Nie, S. Sun, Y.-B. He, W. Ren, B. Li, F. Kang, J.-K. Kim, T.-Y. Zhang, *Nano Lett.* **2017**, *17*, 1282.
- [20] E. Bêche, P. Charvin, D. Perarnau, S. Abanades, G. Flamant, *Surf. Interface Anal.* **2008**, *40*, 264.
- [21] Z. Zhang, D. Han, S. Wei, Y. Zhang, *J. Catal.* **2010**, *276*, 16.
- [22] N. S. Arul, D. Mangalaraj, R. Ramachandran, A. N. Grace, J. I. Han, *J. Mater. Chem. A* **2015**, *3*, 15248.
- [23] A. N. Kravtsova, A. A. Guda, J. Goettlicher, A. V. Soldatov, V. K. Taroev, A. A. Kashae, L. F. Suvorova, V. L. Tauson, *J. Phys.: Conf. Ser.* **2016**, *712*, 012096.
- [24] L. Truffault, M.-T. Ta, T. Devers, K. Konstantinov, V. Harel, C. Simonard, C. Andrezza, I. P. Nevirkovets, A. Pineau, O. Veron, J.-P. Blondeau, *Mater. Res. Bull.* **2010**, *45*, 527.
- [25] S. Phoka, P. Laokul, E. Swatsitang, V. Promarak, S. Seraphin, S. Maensiri, *Mater. Chem. Phys.* **2009**, *115*, 423.
- [26] P. A. Montano, J. Zhao, M. Ramanathan, G. K. Shenoy, W. Schulze, in *Small Particles and Inorganic Clusters* (Eds: C. Chapon, M. F. Gillet, C. R. Henry), Springer, Berlin, Heidelberg **1989**, pp. 103–105.
- [27] N. A. Young, *Coord. Chem. Rev.* **2014**, *277–278*, 224.
- [28] A. Balerna, E. Bernieri, P. Picozzi, A. Reale, S. Santucci, E. Burattini, S. Mobilio, *Phys. Rev. B* **1985**, *31*, 5058.
- [29] P. A. Montano, Y. Cao, *J. Phys.: Condens. Matter* **1993**, *5*, A209.
- [30] H.-G. Fritsche, R. E. Benfield, *Z. Phys. D: At., Mol. Clusters* **1993**, *26*, 15.
- [31] A. I. Frenkel, A. Yevick, C. Cooper, R. Vasic, *Annu. Rev. Anal. Chem.* **2011**, *4*, 23.
- [32] G. Giuli, A. Trapananti, F. Mueller, D. Bresser, F. d'Acapito, S. Passerini, *Inorg. Chem.* **2015**, *54*, 9393.
- [33] G. Giuli, T. Eisenmann, D. Bresser, A. Trapananti, J. Asenbauer, F. Mueller, S. Passerini, *Materials* **2018**, *11*, 49.
- [34] Y. Ma, Y. Ma, D. Bresser, Y. Ji, D. Geiger, U. Kaiser, C. Streb, A. Varzi, S. Passerini, *ACS Nano* **2018**, *12*, 7220.
- [35] M. R. Lukatskaya, B. Dunn, Y. Gogotsi, *Nat. Commun.* **2016**, *7*, 12647.
- [36] Y. Ma, Y. Ma, G. Giuli, T. Diemant, R. J. Behm, D. Geiger, U. Kaiser, U. Ulissi, S. Passerini, D. Bresser, *Sustainable Energy Fuels* **2018**, *2*, 2601.
- [37] Y. Ma, Y. Ma, U. Ulissi, Y. Ji, C. Streb, D. Bresser, S. Passerini, *Electrochim. Acta* **2018**, *277*, 100.
- [38] X. Su, J. Liu, C. Zhang, T. Huang, Y. Wang, A. Yu, *RSC Adv.* **2016**, *6*, 107355.
- [39] X. Sun, X. Zhang, B. Huang, H. Zhang, D. Zhang, Y. Ma, *J. Power Sources* **2013**, *243*, 361.
- [40] A. Varzi, D. Bresser, J. von Zamory, F. Müller, S. Passerini, *Adv. Energy Mater.* **2014**, *4*, 1400054.
- [41] W. Wang, D. Choi, Z. Yang, *Metall. Mater. Trans. A* **2013**, *44*, 21.
- [42] L. Shen, H. Lv, S. Chen, P. Kopold, P. A. van Aken, X. Wu, J. Maier, Y. Yu, *Adv. Mater.* **2017**, *29*, 1700142.
- [43] H. Kim, M.-Y. Cho, M.-H. Kim, K.-Y. Park, H. Gwon, Y. Lee, K. C. Roh, K. Kang, *Adv. Energy Mater.* **2013**, *3*, 1500.
- [44] V. Aravindan, J. Sundaramurthy, A. Jain, P. S. Kumar, W. C. Ling, S. Ramakrishna, M. P. Srinivasan, S. Madhavi, *ChemSusChem* **2014**, *7*, 1858.
- [45] J. Xu, Y. Li, L. Wang, Q. Cai, Q. Li, B. Gao, X. Zhang, K. Huo, P. K. Chu, *Nanoscale* **2016**, *8*, 16761.
- [46] A. C. Larson, R. B. Von Dreele, MS-H805, Los Alamos National Laboratory, Los Alamos, NM **1998**.
- [47] C. Artini, M. Pani, M. M. Carnasciali, M. T. Buscaglia, J. R. Plaisier, G. A. Costa, *Inorg. Chem.* **2015**, *54*, 4126.
- [48] F. d'Acapito, G. O. Lepore, A. Puri, A. Laloni, F. La Manna, E. Dettona, A. De Luisa, A. Martin, *J. Synchrotron Radiat.* **2019**, *26*, 551.
- [49] A. Puri, G. O. Lepore, F. d'Acapito, *Condens. Matter* **2019**, *4*, 12.
- [50] P. A. Lee, P. H. Citrin, P. Eisenberger, B. M. Kincaid, *Rev. Mod. Phys.* **1981**, *53*, 769.
- [51] B. Ravel, M. Newville, *J. Synchrotron Radiat.* **2005**, *12*, 537.
- [52] B. Ravel, *J. Synchrotron Radiat.* **2001**, *8*, 314.
- [53] A. L. Ankudinov, B. Ravel, J. J. Rehr, S. D. Conradson, *Phys. Rev. B* **1998**, *58*, 7565.
- [54] T. P. Gujar, V. R. Shinde, C. D. Lokhande, R. S. Mane, S.-H. Han, *Appl. Surf. Sci.* **2005**, *250*, 161.
- [55] M. Kuenzel, G.-T. Kim, D. Bresser, S. Passerini, *ECS Meet. Abstr.* **2018**, *MA2018-02*, 223.
- [56] D. Bresser, E. Paillard, R. Kloepsch, S. Krueger, M. Fiedler, R. Schmitz, D. Baither, M. Winter, S. Passerini, *Adv. Energy Mater.* **2013**, *3*, 513.
- [57] G. Kresse, J. Furthmüller, *Phys. Rev. B* **1996**, *54*, 11169.
- [58] G. Kresse, D. Joubert, *Phys. Rev. B* **1999**, *59*, 1758.
- [59] J. P. Perdew, K. Burke, M. Ernzerhof, *Phys. Rev. Lett.* **1996**, *77*, 3865.
- [60] W. Tang, E. Sanville, G. Henkelman, *J. Phys.: Condens. Matter* **2009**, *21*, 084204.
- [61] E. Sanville, S. D. Kenny, R. Smith, G. Henkelman, *J. Comput. Chem.* **2007**, *28*, 899.
- [62] G. Henkelman, A. Arnaldsson, H. Jónsson, *Comput. Mater. Sci.* **2006**, *36*, 354.
- [63] M. Yu, D. R. Trinkle, *J. Chem. Phys.* **2011**, *134*, 064111.